

On the challenges in experimental characterization of flow separation over airfoils at low Reynolds number

David A. Olson · Alan W. Katz · Ahmed M. Naguib ·
Manoochehr M. Koochesfahani · Donald P. Rizzetta ·
Miguel R. Visbal

Received: 15 September 2012 / Revised: 13 January 2013 / Accepted: 24 January 2013 / Published online: 12 February 2013
© Springer-Verlag Berlin Heidelberg 2013

Abstract Measurements and computations of the separation and reattachment locations are reported for the steady flow over a SD7003 airfoil at different angles of attack and chord Reynolds number in the range 2×10^4 – 4×10^4 . The experiments are based on multi-line molecular tagging velocimetry, and the computations employ an implicit large eddy simulation approach. Comparisons of experimental results with current computations and previous experiments point to challenges involved in the experimental determination of the separation bubble characteristics. The results also underline the importance of the facility-dependent freestream turbulence level on the experimental data. The collective effect of experimental uncertainty and facility-dependent issues, examined systematically herein, appear to clarify the discrepancy among the various experimental and computational results. The findings also suggest that accurate characterization of the separation bubble over airfoils at low Reynolds number is more difficult than generally recognized and presents a challenge in comparing results between different experiments, and between experiments and computations. Moreover, this complicates the validation of computational data against experiments within this flow regime.

1 Introduction

The low Reynolds number flows found in Micro Air Vehicles (MAVs), wind turbines and bio-mimetic applications are highly susceptible to the development of the Laminar Separation Bubble (LSB) under even small adverse pressure gradients. This fundamental flow phenomenon in aerodynamics has been heavily studied with an increasing emphasis in recent years; for example, see Ol et al. (2005), Radespiel et al. (2006), Burgmann et al. (2007), Burgmann and Schröder (2008), Galbraith and Visbal (2010), and Katz (2010). In the present work, we investigate the characteristics of the LSB on the steady SD7003 airfoil at different angles of attack (α) over a chord (c) Reynolds number (Re_c) in the range 2×10^4 – 4×10^4 . The specific focus is on determining the separation and reattachment locations (x_S and x_R , respectively).

Previous studies of this airfoil point to discrepancies among data sets compiled in different investigations. For example, Ol et al. (2005) reported measurements of x_S and x_R in three different facilities for the flow over an SD7003 at an angle of attack of 4° and $Re_c = 6 \times 10^4$. The results showed substantial variation in x_S/c between 0.18 and 0.33 (i.e., a difference of 15 % of the chord length). The variation in x_R/c was less pronounced, falling within the range 0.58–0.63. Ol et al. (2005) hypothesized these discrepancies were due to minor differences in angle of attack and freestream turbulence levels between the different facilities and also suggested the differences found in the flow structure of the separation bubble were due to inadequate spatial resolution and/or the temporal PIV sampling rate. The influence of freestream turbulence intensity (FSTI) is likely very important since it acts as a broadband excitation source of the boundary layer instability upstream of separation and the Kelvin–Helmholtz instability downstream,

D. A. Olson · A. W. Katz · A. M. Naguib (✉) ·
M. M. Koochesfahani
Mechanical Engineering, Michigan State University,
East Lansing, MI 48824, USA
e-mail: naguib@egr.msu.edu

D. P. Rizzetta · M. R. Visbal
U.S. Air Force Research Laboratory, Wright-Patterson Air Force
Base, Dayton, OH 45433-7512, USA

which may delay separation while triggering earlier transition and subsequent turbulent reattachment. This would have the effect of shortening the laminar separation bubble with increased FSTI. Burgmann and Schröder (2008), comparing to their earlier results (e.g., Burgmann et al. 2007) at a higher FSTI, observed a downstream shift in separation location and thinning LSB with increased FSTI. They also found structurally similar, but smaller, vortical patterns in the LSB for the higher FSTI result.

In the work presented here, the difficulty in accurately determining the separation and reattachment locations of separation bubbles over airfoils at low Reynolds number is further underlined through coordinated experimental and computational investigations of the flow over the SD7003 airfoil. As will be seen, comparison between the results from both of these investigations, as well as with the experimental results of Burgmann et al. (2007) and Burgmann and Schröder (2008), for the same Reynolds number and angle of attack, exhibit a great deal of variation. This leads us to methodically examine the sensitivity of the uncertainty in determination of the separation and reattachment locations to various factors: angle of attack, Reynolds number, near-wall spatial resolution, and FSTI. Ultimately, this undertaking highlights the experimental challenges that impact the accurate characterization of the separation bubble.

2 Experiments

The experimental facility at the Turbulent Mixing and Unsteady Aerodynamics Laboratory at Michigan State University is a 10,000-l closed-loop free-surface water tunnel (Engineering Laboratory Design, ELD) with full optical access to its 61 cm \times 61 cm \times 244 cm test section. The flow management consists of two perforated-plate baffles and one honeycomb in the settling chamber, a 6:1

contraction, and a honeycomb and a fine mesh screen at the entrance of the test section.

The SD7003 airfoil, depicted in Fig. 1, has a nominal chord and span of $c = 20.3$ cm and $b = 46.0$ cm, respectively, for a geometric aspect ratio of 2.3. The airfoil, which is the same airfoil used by Ol et al. (2005) in the Air Force Research Laboratory experiments and in Katz (2010), is mounted between acrylic false walls and centered in the test section. The angle of attack is controlled using a lever located on the outside of one of the false walls with an accuracy of $\pm 0.4^\circ$ (the procedure to determine the angle is described later in the document).

Single-component Molecular Tagging Velocimetry (1c-MTV), as shown in Fig. 2, is utilized for flow velocity measurements. MTV can be considered as the molecular counterpart of PIV (Particle Image Velocimetry). In the present implementation of MTV, an Excimer UV laser (Lambda Physik LPX 210i XeCl 308 nm) is fired once to excite ("tag") a supramolecule tracer (see Gendrich et al. 1997) mixed with the water in the test facility and the resulting phosphorescence emission from the tracer is interrogated twice with a prescribed time delay to form an image pair. Correlation analysis of the image pair yields the velocity component perpendicular to the tag line in the undelayed image (Fig. 2a) for each tag line and each row of the image. In the present work, this corresponds to the velocity component parallel to the freestream direction. The random uncertainty of the correlation technique, based on the RMS (root mean square), is nominally 0.05 pixels for typical measurements (Gendrich et al. 1996). The reader is referred to Gendrich et al. (1996) for additional details on processing and Koochesfahani and Nocera (2007) for further details on the MTV technique.

The results reported here are generated from two different experiments. The first focuses on the effect of Re_c and α on separation and reattachment locations of the LSB; the second addresses the influence of FSTI on the LSB

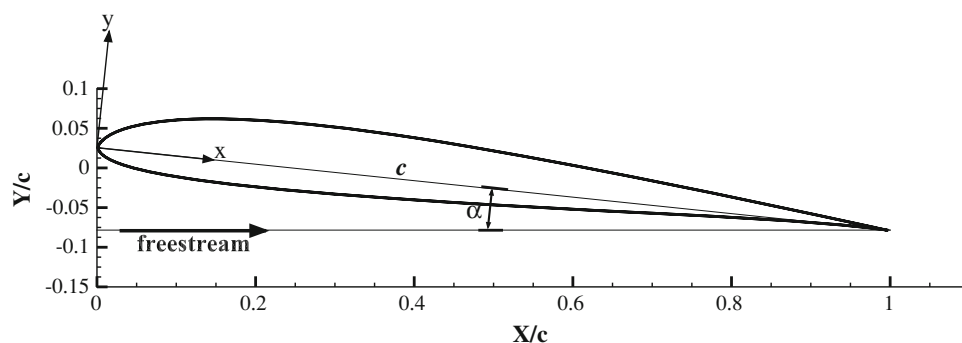


Fig. 1 Airfoil profile, geometric parameters, and the frames of reference are depicted above. The angle of attack, α , is the angle between the *chord line* and the freestream velocity vector. The coordinates (X, Y) are designated as the lab reference frame where the

streamwise component of velocity (U) is along the X direction. The coordinate system designated by (x, y) is the airfoil frame of reference (i.e., *chord line* is aligned with the x -axis)

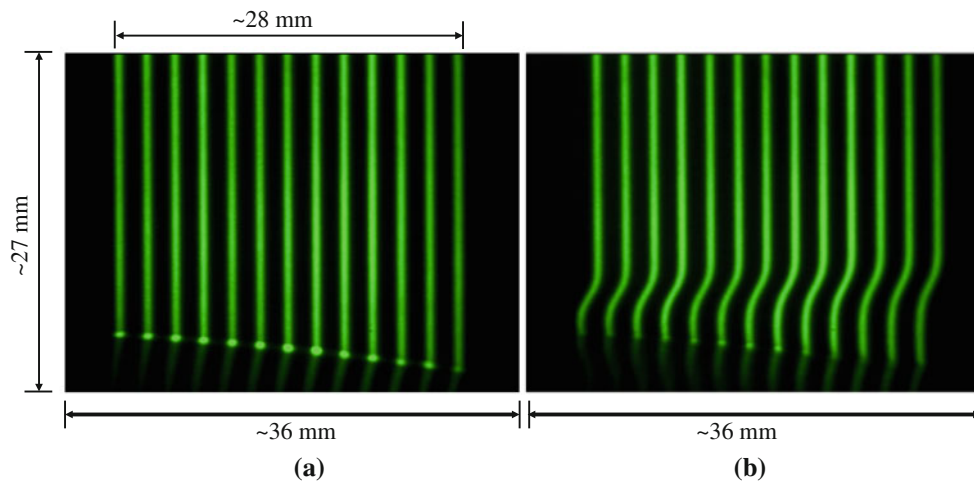
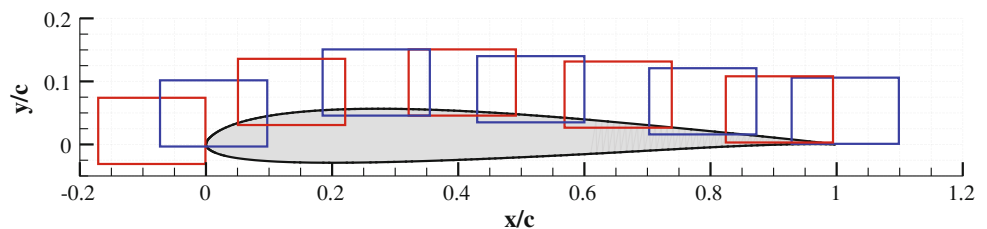


Fig. 2 Example of 1c-MTV image pair near the surface of an SD7003 airfoil at $\alpha = 6^\circ$, $Re_c = 2 \times 10^4$. The image extends in the streamwise direction from ~ 0.2 to $0.4 c$. **a** The undelayed image is

shown $2 \mu\text{s}$ after the laser pulse. **b** The delayed image, taken 10 ms later, shows the instantaneous streamwise velocity profile

Fig. 3 Ten overlapping fields of view were used to capture the near-surface flow. Additional fields of view were added above those depicted to capture the entire shear layer, as needed, and the freestream conditions



characteristics. The details of each experiment are presented in the following sub-sections.

2.1 Experiment # 1

The sample image pair in Fig. 2 is acquired using a Stanford Computer Optics (SCO) 4QuikE intensified CCD camera in dual-frame mode at 30 Hz with a resolution of 640×480 pixels. The undelayed image is captured $2 \mu\text{s}$ after the laser pulse, to avoid capturing the bright fluorescence that occurs during excitation, and the time delay between images (5 ms) is selected such that the displacement of a tagged line of fluid in the freestream is nominally half the streamwise line spacing of 1.65 mm, or 8.13 mc (we define the term “millichord,” as one-thousandth of a chord to facilitate the discussion of the small quantities of interest, that is, $8.13 \text{ mc} = 0.00813 c$), in the streamwise direction; which is also the streamwise measurement resolution. The cross-stream resolution is $58 \mu\text{m}$, or 0.29 mc , along the tag line (a factor of nearly 10 improvement in resolution over the recent PIV measurements by Burgmann et al. (2007) and Burgmann and Schröder (2008) for a similar flow field).

To attain the high spatial resolution reported above, the field of view (FOV) is restricted to only a fraction of the entire flow field; typically $0.18 c \times 0.14 c$. Measurements

from twelve such fields of view, ten of which are shown over the surface of the airfoil in Fig. 3, are combined to form a composite view of the results, for example see Fig. 6a. The strength of the single-component MTV is its ability to make high-resolution, near-wall measurements, which, as will be shown, is needed for accurate characterization of the thin separation bubble found on the SD7003 airfoil at low angles of attack at the Reynolds numbers considered. In Katz (2010), a time series of 750 images obtained over a 150-s interval was determined to be sufficient for statistical convergence of the mean velocity (with the random uncertainty less than 1 % in the free-stream and less than 4 % in the separated shear layer). These images were used to obtain ensemble-averaged velocity fields used in the present investigation.

The geometric angle of attack is determined by a least-squares minimization of the error between the airfoil surface location and the theoretical SD7003 profile. The surface is manually located by the intersection of each laser line with the surface, with the center of the bright spot (see the image in Fig. 2a) used as the surface location. The repeatability of visually determining the surface by this method is ± 1 pixel. The maximum and RMS deviation between the actual and theoretical suction-side airfoil profile are found to be less than 0.2 mm (1 mc) and 0.1 mm (0.5 mc), respectively, at the measurement plane.

Table 1 The values of angle of attack and chord Reynolds number for the first set of experiments

Angle of attack α	Chord Reynolds number Re_c
3.8°, 5.7°, 7.3°, 8.8°, 10.6°	2.1×10^4
3.5°, 7.4°	3.2×10^4
3.6°, 5.5°, 7.3°, 10.4°	4.6×10^4

Using this approach, the uncertainty in the geometric angle of attack is $\pm 0.4^\circ$, and this process clarifies why the actual measured angle of attack deviates from the intended integer values.

All measurements are conducted over a plane that is located close to mid-span for nominal Re_c values of 2×10^4 , 3×10^4 , and 4×10^4 and angles of attack in the nominal range 3° – 11° , with the actual values tabulated in Table 1.

2.2 Experiment # 2

The influence of freestream turbulence intensity on separation and reattachment is determined with a similar experimental setup as described above, but after the introduction of a turbulence-generating grid at approximately two chord lengths upstream of the airfoil leading edge. The FSTI is defined as the ratio of the RMS of the streamwise velocity fluctuations in the freestream to the freestream velocity: $FSTI \equiv u_{rms}/U_\infty$. The FSTI is measured at $X \approx 0c$ and $Y \approx 0.5c$ for this experiment. The grid is made from a stainless steel-woven mesh with a mesh size of 19.1 mm (0.75 in.) and a wire diameter of 3.0 mm (0.12 in.). In the absence of the grid, the baseline FSTI in the frequency band 0.8–6.5 Hz is 0.3 %. The presence of the grid increases the FSTI in the same frequency band to 0.9 %. The overall FSTI (i.e., the entire frequency range) is approximately 1.9 and 2.2 % for the baseline and added FSTI configurations, respectively, with most of the fluctuation originating from low-frequency oscillations of less than 0.12 Hz (which is unaffected by the presence of the grid).

This set of experiments utilize a 12-bit $1,392 \times 1,024$ pixel PCO Pixelfly QE camera paired with a Nikkor 50 mm f/1.2 lens. This camera does not have the capability of recording two images in short succession in dual-frame mode; therefore, there are no longer individual image pairs but two sequences of images recorded at two different time delays relative to the laser pulse. The first (undelayed) image sequence is recorded approximately 30 μ s after the laser pulse. The second (delayed) image sequence is captured at a time delay of 10.3 ms after the laser pulse. For computing the freestream turbulence characteristics, the

delayed image is captured at 12.3 ms relative to the laser pulse. The spatial resolution of the measurements is kept nominally the same as that used for measurements without the turbulence-generating grid.

In this experiment, data are acquired for the baseline configuration and the flow with added FSTI at an identical geometric angle of attack and freestream velocity difference of less than 4 %. The nominal Re_c is 2.5×10^4 and the geometric angle of attack is approximately 6° . The Reynolds number for the case with added FSTI is about 4 % lower than that for the baseline configuration.

2.3 Error analysis of experimental method

Single-component MTV has an inherent measurement uncertainty due to the unknown velocity component parallel to the tag line (v). This uncertainty, which is described in further detail in Koochesfahani and Nocera (2007), may be formally expressed as (see Hill and Klewicki 1996):

$$\frac{\Delta u}{u} = \frac{v}{u} \frac{\partial u}{\partial y} \Delta t \quad (1)$$

where y is the direction along the tag line (also the cross-stream direction in the present work), and Δt is the time delay between the image pair. From Eq. [1], it is clear that the error in measuring u approaches zero near surfaces, where the ratio $v/u \rightarrow 0$, and in the freestream, where v/u and $\partial u/\partial y \rightarrow 0$. Reducing Δt also decreases the error; however, this is constrained by the required line displacement between the undelayed and delayed images for optimal measurement accuracy.

In order to estimate the error using 1c-MTV in the specific flow under consideration, “simulated experiments” are conducted using the CFD data from Galbraith and Visbal (2008) at $Re_c = 4 \times 10^4$ and $\alpha = 4^\circ$. Other flow conditions (Re_c and α) are also studied leading to similar conclusions as the case presented and are excluded for brevity. In the simulated experiments, the mean velocity field from the CFD simulation is utilized to provide the flow field in which the “experiments” will be performed. Using this velocity field, the Lagrangian displacement of prescribed fluid particle locations, analogous to those comprising the tagged line of fluid molecules in the “undelayed image” of the real experiment, are tracked in time. The cross-stream resolution and streamwise spacing of the initial fluid particles are similar to those of the real experiments. Each particle is then displaced using the known (i.e., computed from CFD) local velocity vector over a time period equal to a typical experimental value of Δt (the time between image pairs). The final locations of the tracked fluid particles yield the simulated “delayed image.” The simulated displacement measurement at a given y location is determined from the streamwise spacing

between the undelayed and delayed tagged lines of fluid at that given y location. The corresponding “measured” velocity is determined by dividing the displacement by Δt .

Once the simulated-MTV-measured velocity is obtained, the corresponding error due to any deviation from the true underlying velocity field is computed. The error is found by remapping the known (true) CFD velocity field onto the “measurement grid” (i.e., the locations of the tracked fluid particles on the undelayed line), and the difference between the “measured” and true streamwise velocity component is computed. The magnitude of the error between the streamwise velocity component obtained from the CFD velocity and that computed from the simulated experiment, normalized by the freestream velocity, is shown in Fig. 4 for $\Delta t = 5$ ms. Over most of the flow field, a negligible error is found, with the highest values occurring near the leading edge due to the very high velocity gradients and large v in this region. The error in the separated shear layer, extending from approximately 0.24 – 0.7 c , is less than 0.9 % in Fig. 4, and it is estimated to be less than 2 % for all the cases in the current experiments.

3 Computations

For the present airfoil simulations, the governing equations are the unfiltered full compressible Navier–Stokes equations cast in strong conservative form after introducing a general time-dependent curvilinear coordinate transformation $(x, y, z, t) \rightarrow (\xi, \eta, \zeta, \tau)$ from physical to computational space. In terms of non-dimensional variables, these equations can be written in vector notation as.

$$\frac{\partial Q}{\partial \tau} + \frac{\partial F_1}{\partial \xi} + \frac{\partial G_1}{\partial \eta} + \frac{\partial H_1}{\partial \zeta} = \frac{1}{\text{Re}} \left[\frac{\partial F_v}{\partial \xi} + \frac{\partial G_v}{\partial \eta} + \frac{\partial H_v}{\partial \zeta} \right] \quad (2)$$

$$Q = \frac{1}{J} [\rho, \rho v, \rho v, \rho w, \rho E]^T \quad (3)$$

here Q , shown in Eq. [3], denotes the solution vector and J is the transformation Jacobian. The inviscid and viscous fluxes can be found, for instance, in Anderson et al. (1984). In the expressions above, u, v, w are the Cartesian velocity components, ρ the density, p the pressure, and T the temperature. The perfect gas relationship $p = \rho T / (\gamma M^2)$,

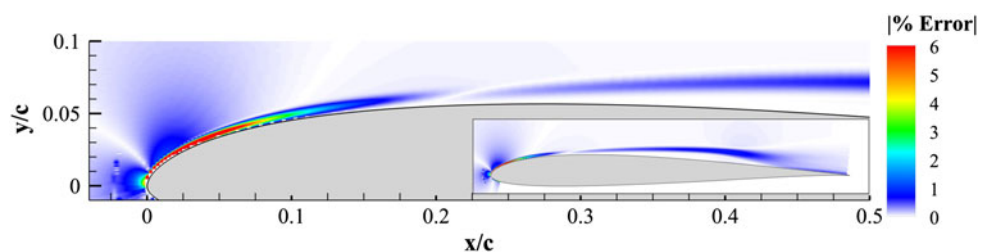
Sutherland’s law for viscosity, and a constant molecular Prandtl number ($Pr = 0.72$) are also assumed.

It should be noted that the above-governing equations correspond to the original *unfiltered* Navier–Stokes equations and are used without change in laminar, transitional, or fully turbulent regions of the flow. Unlike the standard LES approach, no additional sub-grid stress (SGS) and heat flux terms are appended. Instead, a high-order low-pass filter operator is applied to the conserved dependent variables during the solution of the standard Navier–Stokes equations. This highly discriminating filter selectively damps only the evolving poorly resolved high-frequency content of the solution. This filtering regularization procedure provides an attractive alternative to the use of standard SGS models and has been found to yield suitable results for several canonical turbulent flows (Visbal and Rizzetta 2002; Visbal et al. 2003) on LES-level grids.

All simulations are performed employing the extensively validated high-order *FDL3DI* Navier–Stokes solver, described in more detail in (Visbal and Gaitonde 1999 and 2002). In this code, a finite-difference approach is used to discretize the governing equations, and all spatial derivatives are obtained employing a 6th-order compact-differencing scheme. In order to eliminate high-frequency spurious components, an 8th-order Pade-type low-pass spatial filtering operator (Visbal and Gaitonde 1999, 2002) is also incorporated. This filter is applied to the conserved variables along each transformed coordinate direction after each time step or sub-iteration. For transitional and turbulent flows, this filtering technique provides an effective implicit LES approach, as previously noted.

The original airfoil sharp trailing edge is rounded with a circular arc of radius $r/c \approx 0.0004$ in order to facilitate the use on an O-mesh topology. The computational mesh, Fig. 5, consists of $(651 \times 395 \times 151)$ points in the streamwise, normal, and spanwise direction, respectively. The entire domain extends approximately ± 100 c lengths in the streamwise and normal directions, with grid points concentrated near the airfoil in order to capture the transition process. For the three-dimensional simulations, which invoke periodicity in the spanwise direction, the mesh has a span $s/c = 0.2$. A very small computational time step $(\Delta t u_\infty)/c = 0.0001$ is prescribed in order to provide sufficient temporal resolution of the fine-scale

Fig. 4 A detailed view of the estimated 1c-MTV measurement error shown as $|\Delta U|/U_\infty \times 100$ with the inset image showing the entire suction side of the airfoil ($Re_c = 4 \times 10^4$, $\alpha = 4^\circ$)



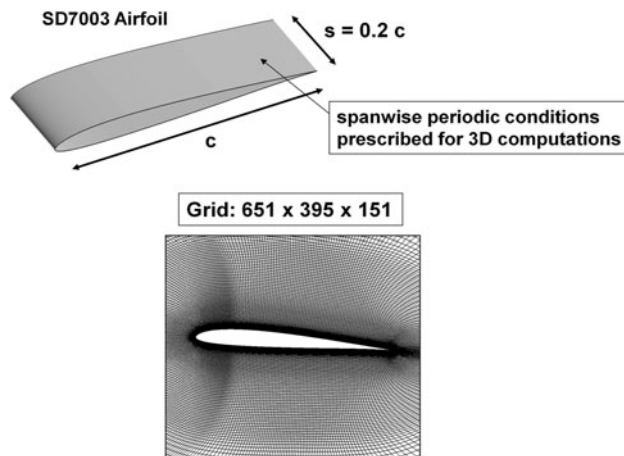


Fig. 5 The airfoil section and mesh for the computational study is shown. The grid density has been reduced for clarity

Table 2 The values of angle of attack and chord Reynolds number for the computations

Angle of attack α	Chord Reynolds number Re_c
3.6°	4.2×10^4
4.0°	4.0×10^4

fluctuations. Simulations are advanced in time for a total of 200,000 time steps with mean and RMS data collected during the last 100,000 iterations. Finally, all computations are performed employing a low freestream Mach number $M = 0.1$, as required with the present compressible Navier–Stokes solver. At the moderate angles of attack considered, see Table 2, compressibility effects in the computations are found to be negligible. For instance, at $\alpha = 8^\circ$ and $Re_c = 4 \times 10^4$, the maximum variation in the time-averaged density was found to be $<2\%$.

4 Results and discussion

4.1 Separation and reattachment locations

A typical whole-field mean velocity map from the current measurements is illustrated in Fig. 6a for the particular case of $Re_c = 4 \times 10^4$ and $\alpha = 3.6^\circ$. To aid the identification of the separation bubble location, negative mean velocity is labeled by black color. One can clearly see the presence of a thin separation bubble over the airfoil surface. The corresponding computation for this case is shown in Fig. 6b; black color again highlights the reversed flow region. Overall, there is a good qualitative agreement between the two sets of results, but we also note subtle differences. The apparent location of the separation point is

different, with the experiment indicating a farther downstream location. The maximum height of the LSB and where it occurs are also different; the experiment shows a thinner separation bubble with its maximum height farther downstream than in the computation.

The streamwise locations of separation and reattachment are estimated based on the mean velocity reversal at the first velocity measurement above the surface. For the measurements reported here, the first reliable velocity measurement is typically located between five and ten pixels above the surface, below which the near-surface glow caused by phosphorescence emission from impurities in the coating of the airfoil surface (see the bright spots in Fig. 2a) locally corrupts the correlation routine. Proper surface treatment will mitigate or eliminate this issue, which has been done in the follow-up studies of Olson (2011).

The separation location is found by identifying the position along the surface above which the velocity first reverses its direction. The separation point is chosen to be between this location and the one immediately upstream of it. An example of this is shown in Fig. 7a; in which mean velocity vectors are overlaid onto a mean velocity contour map. Similarly, when looking for the reattachment point, the first profile downstream of separation in which no reverse velocity is found near the surface is sought. An example of how the reattachment point is determined is shown in Fig. 7b. The uncertainty of determining separation and reattachment locations in this fashion is a function of both the streamwise spacing of the tagged lines of fluid molecules and nearest reliable velocity measurement to the surface. The former is easily classified as one-half the line spacing or $\pm 5.5\text{ mc}$ for the current experiment, and the implications of the latter are discussed in detail later.

To quantify the LSB characteristics, comparisons of the separation and reattachment locations at $Re_c = 4 \times 10^4$ obtained from four different experiments/computations are shown in Fig. 8. We note that the figure includes two different sets of AFRL computational results: Galbraith and Visbal (2008) and the current computations, and two sets of experimental results: Burgmann and Schröder (2008) and the current experiments. Burgmann and Schröder (2008) employed PIV measurements with 2.5 mc spatial resolution in the streamwise and cross-stream directions compared to the current MTV resolution of 5.5 and 0.29 mc in the streamwise and cross-stream directions, respectively. The current experimental results represent separation and reattachment locations determined in two ways: (1) from the first reliable velocity vector above the surface (in the region $1.5\text{--}2.9\text{ mc}$); and (2) at one pixel (0.29 mc) above the surface estimated via a polynomial fit to the reliable data and the no-slip boundary condition at the wall. The comparison of the two different methods highlights the importance of

Fig. 6 Comparisons of the mean streamwise velocity obtained from experiment **a** and computation **b** at $Re_c = 4 \times 10^4$ and $\alpha = 3.6^\circ$. The magnitude of the velocity normalized by the freestream velocity is given by the color bar. Note that the black color is used to highlight the zone of negative streamwise velocity to aid in visual identification of the separation bubble

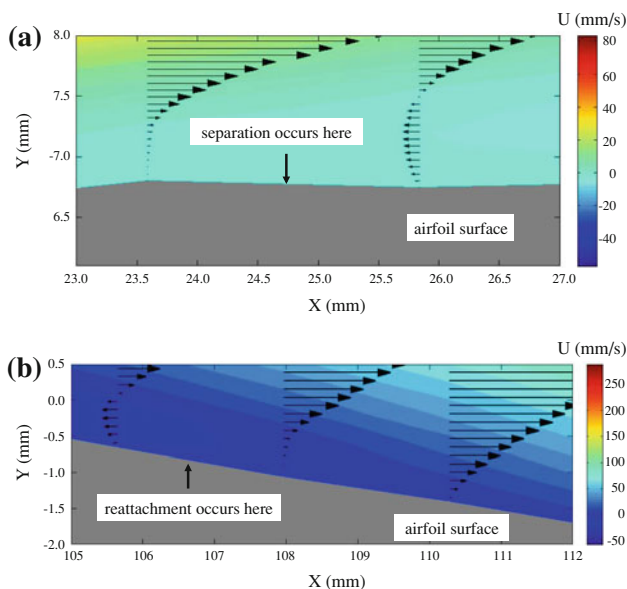
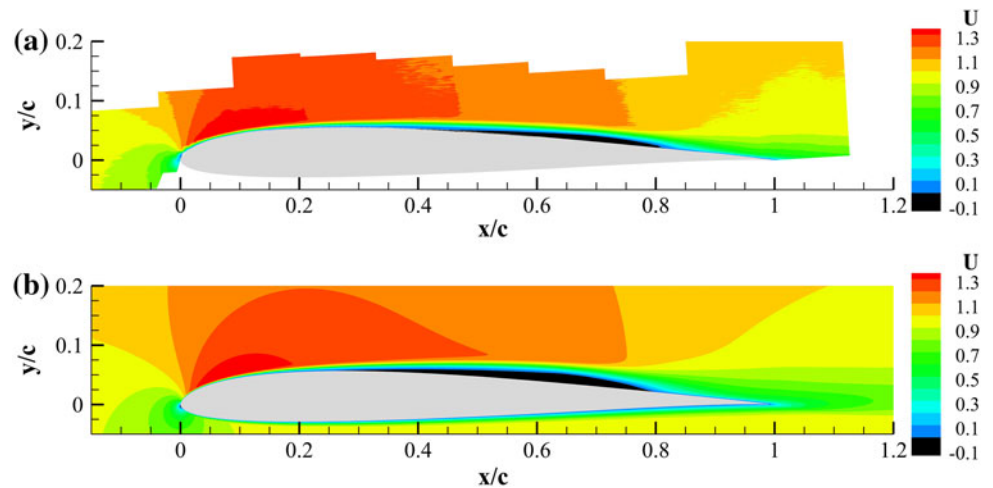


Fig. 7 **a** Mean velocity profiles, between which separation occurs, overlaid on a mean velocity contour map. **b** The same as **a** but near reattachment. Note: not to scale

near-wall spatial resolution, which is discussed in detail later.

The separation locations from the current experiments (based on the first reliable data near the surface) agree very well with the Burgmann and Schröder (2008) results. However, the separation locations in the current experiments, determined by the fitted data are consistently farther upstream compared to those reported by Burgmann and Schröder (2008). All of the experimental results indicate separation points farther downstream when compared to the computations.

Interestingly, however, good agreement is found in the reattachment locations between the computations and current experiments. But, the current experiments show reattachment locations that are consistently farther

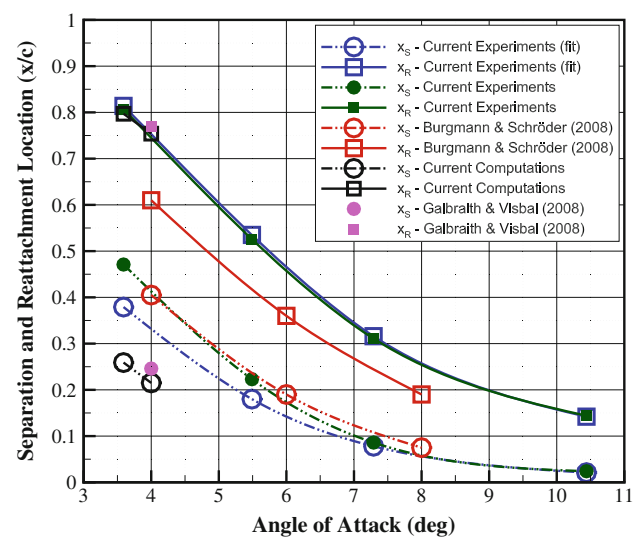


Fig. 8 Comparison of separation and reattachment locations obtained from different studies of the flow over an SD7003 airfoil at a nominal $Re_c = 4 \times 10^4$. A square symbol is used for reattachment location, whereas a circle is used for separation location data. Splines are used to connect points to highlight the trends

downstream than those of Burgmann and Schröder (2008). The larger variation in separation as compared to reattachment location among the different data sets was also observed by Ol et al. (2005) in their comparison of experimental data obtained in different flow facilities at a higher Reynolds number ($Re_c = 6 \times 10^4$) and a single angle of attack of $\alpha = 4^\circ$.

The LSB characteristics for a lower Reynolds number, $Re_c = 2 \times 10^4$, are depicted in Fig. 9. As before, separation and reattachment locations are determined in two ways, from the first reliable velocity vector above the surface and also via a polynomial fit extrapolated to the wall. We note that the latter method leads to a more upstream location for separation point, but has little impact on the reattachment location determination, an effect that is

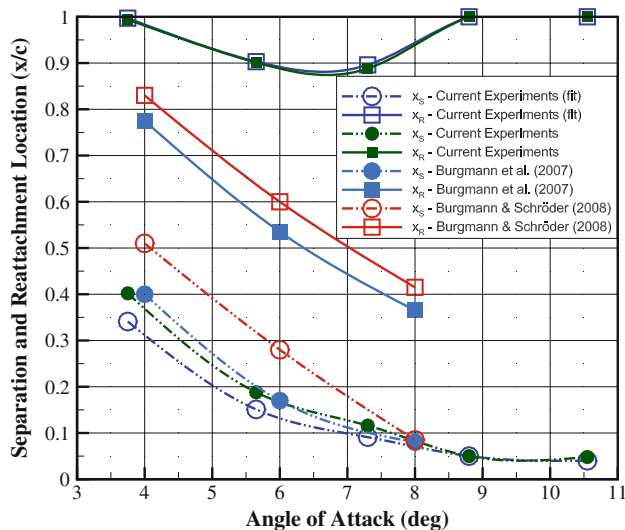


Fig. 9 Comparison of separation and reattachment locations obtained from different studies of the flow over an SD7003 airfoil at a nominal Re_c of 2×10^4 . Reattachment location marked at $x/c = 1$ indicates an *open separation bubble* (i.e., reattachment does not occur over the airfoil surface). A spline is used to connect points to highlight trends

also seen in Fig. 8. In Fig. 9, we compare the current experimental results with the previous data of Burgmann et al. (2007) and Burgmann and Schröder (2008); no corresponding computations were available for comparison. The types of differences between the experimental results noted in Fig. 8 for $Re_c = 4 \times 10^4$ also persist for this lower Reynolds number. We note, however, that the reattachment locations are now significantly different compared to the higher Reynolds number case. In particular, for the lowest and highest two angles of attack at $Re_c = 2 \times 10^4$, the current experiments show completely separated flow with no reattachment and much longer separation bubbles at modest angles. However, both Burgmann et al. (2007) and Burgmann and Schröder (2008) see reattachment across all angles studied with the reattachment location showing a strong dependence on angle of attack. Much of the systematic differences in separation location between the current experiments and the latter two studies discussed from the literature, as well as between the current experiments and computations, may be explained by the discussions that follow.

4.2 Issues in LSB characterization

The discrepancy among the separation and reattachment data shown in Figs. 8 and 9, as well as among the data reported by Ol et al. (2005), implies that the characterization of the LSB at low Reynolds number is more challenging than generally recognized. In the remainder of this document, we bring into focus four specific issues that, individually or in combination, cause difficulty in accurate

experimental characterization of the LSB. Specifically, these issues are (1) strong dependence of the separation and reattachment location on angle of attack at low values of angle of attack; (2) the thinness of the LSB near the separation point and the high spatial resolution required to resolve it; (3) sensitivity to Reynolds number under certain flow conditions; (4) sensitivity of the LSB to freestream turbulence level. In the following, we examine each of these issues and quantify their influence on the accuracy of determining the separation and/or reattachment location.

4.2.1 Uncertainty due to determination of angle of attack

The sensitivity of the separation location to the angle of attack is found to be particularly significant at low angles. This may be discerned, for instance, from the implied slope of a curve passing through the x_s versus α data in Fig. 8. Using the current experiments or computations, this slope is estimated to be approximately $\partial x_s / \partial \alpha \approx 105$ mc/degree at $\alpha = 3.6^\circ$. Thus, the present $\pm 0.4^\circ$ uncertainty in α would produce a corresponding uncertainty in x_s of ± 42 mc (or ± 4.2 % of the chord length). Accordingly, if accuracy of better than 1 % chord length is desired in determining the separation location (or reattachment point; which also exhibits similar sensitivity to α), the angle of attack determination must be better than $\pm 0.1^\circ$. Though such level of accuracy may be achievable in relation to relative changes in the angle of attack, it would be more challenging to accomplish the same for the absolute angle of attack for asymmetric airfoils, such as the SD7003. For these airfoils, identification of the zero angle of attack can not rely on flow- or surface-pressure symmetry between the top and bottom of the airfoil. Instead, the chord line must be aligned with the approach freestream direction. This would require determination of the approach flow direction at each test velocity (to account for changes in blockage by the test section's boundary layers) at a distance sufficiently far upstream of the airfoil to avoid test-model blockage effect on the approach flow angle.

4.2.2 Uncertainty due to near-wall measurement resolution

Another source for the discrepancy in the x_s data obtained in different studies is the near-wall resolution and the ability to discern flow reversal near the surface. Referring to Fig. 10, which shows an enlarged view of the computed results in the region near separation for the case discussed in Fig. 6, the flow reversal region near the wall is extremely “thin” in the wall-normal direction. Unless the experiment has sufficient spatial resolution, the onset of flow reversal will be estimated to be farther downstream. This can be demonstrated quantitatively by capitalizing on

Fig. 10 Enlarged view of the region near separation from the computational results in Fig. 6b. The black color represents negative streamwise velocity while the surface is colored gray

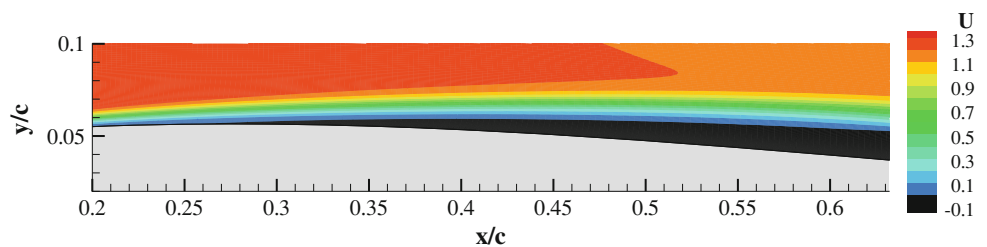
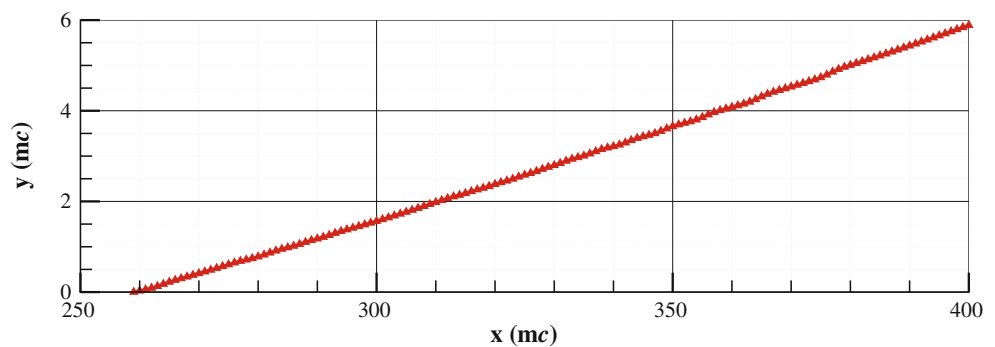


Fig. 11 Dependence of the separation location on the height above the wall where velocity information is used to determine the location of flow reversal. Results are obtained from the computational data shown in Figs. 10 and 6b



the very fine resolution of the present computational results. More specifically, the separation location is determined in the manner described earlier (see Fig. 7) while varying the height above the wall of the node used to determine where flow reversal first occurs. The dependence of the identified separation location on the node height above the wall is plotted in Fig. 11. As seen from the figure, an increasing systematic bias toward the downstream direction is produced with increasing height of the node at which the velocity is used to determine x_S (for an experiment, this would be the location closest to the wall where reliable data are available).

Based on Fig. 11, we determine that if the first velocity data were located 3 mc above the airfoil surface, the estimate of separation location would be shifted downstream by 77 mc (i.e., 7.7 % of the chord length) for the case shown in Figs. 6 and 10. Previous studies, Burgmann et al. (2007) and Burgmann and Schröder (2008), had a spatial resolution of 3.0 and 1.5 mc, respectively, and the studies of Ol et al. (2005) had spatial resolutions ranging from 0.8 to 2.2 mc. However, the near-surface resolution is not explicitly discussed. Some of the studies in Ol et al. (2005) for $Re_c = 6 \times 10^4$ and $\alpha = 4^\circ$ reported separation and reattachment locations despite lacking reversed flow in the mean flow field. The absence of the reversed flow may be due to insufficient near-wall spatial resolution, or more significantly, a separation bubble may not exist all together. Even though the current MTV results have much improved spatial resolution of 0.29 mc, the reliable data nearest to the wall are between 1.5 and 2.7 mc (0.28–0.55 mm). The locations of x_S and x_R determined from the *velocity profile fit* near the surface in the experiments also demonstrate the

effect of near-wall spatial resolution: the location of x_S at $\alpha \approx 3.6^\circ$ shifts upstream by 110mc and x_R shifts downstream by 10 mc when using the fit. Therefore, the discrepancy between the experimental and computational x_S data in Fig. 8 can be explained in part by the measurements not being sufficiently close to the wall.

Clearly, data at closer proximity to the wall than any of the experiments discussed, which would be challenging to achieve, are needed for estimating the separation with high accuracy. This effect will become more prominent at lower angle of attack and higher Reynolds number as the separation bubble becomes thinner. A similar difficulty is not found at reattachment since the bubble is not as thin as near separation. In fact, as discussed earlier, the present computational and experimental data agree fairly well when it comes to determining the reattachment location (Fig. 8).

4.2.3 Sensitivity to Reynolds number

For a certain Reynolds number and angle of attack combination, fairly small changes in the Reynolds number are found to cause large influence on the reattachment location. This may be seen in the results shown in Fig. 12, where the separation and reattachment locations are plotted versus Reynolds number; the data include both the current experiments and computations as well as earlier computations by Galbraith and Visbal (2008). As illustrated in Fig. 12 for $\alpha = 8^\circ$, the reattachment location experiences a large change in the range $Re_c = 2 \times 10^4$ – 3×10^4 . Below this Reynolds number, a very long separation bubble, reattaching near the trailing edge (or remaining open), is found. At higher Reynolds numbers, a much shorter

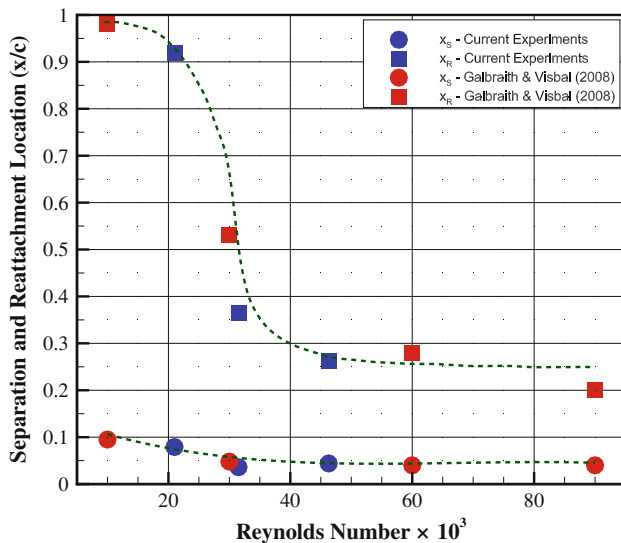


Fig. 12 Dependence of the separation and reattachment location on Reynolds number at $\alpha = 8^\circ$. The current experiments have been interpolated for comparison at $\alpha = 8^\circ$. The dashed green lines are used to highlight the trends only

separation bubble is established (not extending beyond 30 % chord). Though the cause of this large difference over a relatively narrow Reynolds number range is not precisely known, it is believed to be the result of the separated shear layer remaining laminar before reattachment for $Re_c < 3 \times 10^4$, but becoming turbulent for $Re_c > 3 \times 10^4$. Regardless of the source of this high sensitivity to Reynolds number, it is clear that if measurements are conducted at a combination of Reynolds number and angle of attack where such high sensitivity is observed, the results from different investigations could vary significantly if the Reynolds number is not matched precisely. Moreover, if the sensitivity does arise from the transitional state of the shear layer, then facility background disturbances would affect the specific Reynolds number range over which large variation in x_R takes place. Overall, this issue could contribute to the discrepancy between data sets reported in different investigations.

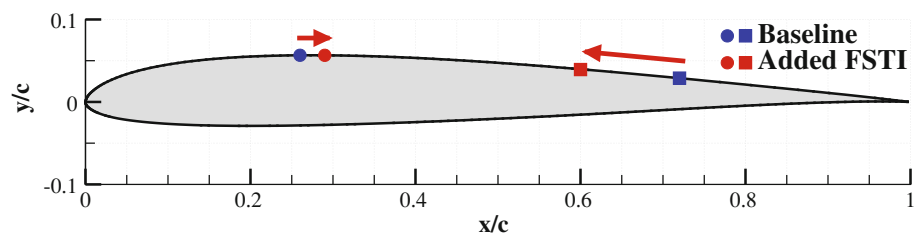
4.2.4 Effect of freestream turbulence

As described in section II, to assess the potential influence of freestream turbulence intensity (FSTI), an experiment is

carried out where a turbulence-generating grid is placed two chord lengths upstream of the airfoil leading edge. The addition of the grid increases the FSTI from 0.3 to 0.9 % in the frequency band 0.8–6.5 Hz. The experiment is conducted twice at $Re_c \approx 2.5 \times 10^4$ and $\alpha \approx 6^\circ$, with and without the grid. Single-component MTV data are obtained as described previously and the locations of separation and reattachment are obtained. The results are summarized in Fig. 13, where it is seen that the separation location moves slightly downstream (by 30 mc or 3 % of the chord length), whereas the reattachment location moves noticeably upstream (by 120 mc or 12 % of the chord length) as a result of added FSTI. The slight difference in Re_c between the two runs does not influence the conclusions drawn here. The influence of the small (about 4 %) reduction in Re_c for the case with increased FSTI, would be expected to be a downstream shift in the reattachment point (see Fig. 12), which is opposite of what is actually measured. The separation point, however, would be expected to move downstream due to Re_c reduction. Based on the sensitivity of separation location to Reynolds number from data in Fig. 12, we estimate the small difference in Re_c to account for only 3 mc out of the measured 30 mc shift in x_S location.

The results in Fig. 13 are consistent with the physical expectation that increased FSTI would result in earlier transition of the shear layer, and hence earlier reattachment. Similarly, an earlier transition of the boundary layer would delay separation. It may be surprising that transition issues would become important at a Reynolds number that is two orders of magnitude below that typical of Blasius boundary layer transition. However, it is well established that the presence of sufficiently high freestream turbulence leads to sub-critical bypass boundary layer transition (e.g., see Matsubara and Alfredsson 2001). It is suspected that such a bypass transition process influences the boundary layer state in the current work, changing it to a more advanced transitional state with a fuller mean velocity profile, leading to the delay of separation. Verification of this hypothesis requires a separate, more detailed investigation. More significantly, however, as far as the present work is concerned, our results demonstrate systematically that the variation of freestream turbulence intensity between different facilities can influence the reported LSB

Fig. 13 Influence of grid-generated freestream turbulence on the locations of separation and reattachment; $Re_c = 2.5 \times 10^4$ and $\alpha \approx 6^\circ$. Closed symbols on the airfoil suction surface mark x_S and x_R



characteristics substantially. This makes it very difficult to compare results obtained in different facilities or between experiments and computations.

A more comprehensive study is underway to examine the influence of freestream turbulence intensity for a broad range of Re_c and α . As part of this study, the influence of FSTI on the separation and reattachment locations, as well as the mean, and more interestingly, the root mean square of the streamwise velocity are under investigation.

5 Conclusion

Concurrent experimental and computational investigations are undertaken to characterize the separation bubble on a steady SD7003 airfoil at low Reynolds numbers. Separation and reattachment locations are compared with previous experiments and current computations. Results reveal several challenges that exist in carrying out such experiments, including the required accuracy for angle of attack measurement, the spatial resolution needed to detect the separation location, and sensitivity to Reynolds number at certain flow conditions and facility-dependent parameters, such as the freestream turbulence level. These issues lead to the conclusion that experimental characterization of the laminar separation bubble over low Reynolds number airfoils is more challenging than generally recognized. This complicates the validation of computational data against experiments in this class of flows.

Acknowledgments This work was supported by the Air Force Research Laboratory (AFRL) through the Michigan/AFRL Collaborative Center for Aeronautical Sciences and, in part, by the Air Force Office of Scientific Research grant number FA9550-10-1-0342. We also thank Dr. Michael Ol of the AFRL at Wright-Patterson Air Force Base for loaning us the SD7003 airfoil used in these experiments.

References

- Anderson DA, Tannehill JC, Pletcher RH (1984) Computational fluid mechanics and heat transfer. McGraw-Hill Book Company, New York
- Burgmann S, Schröder W (2008) Investigation of the vortex induced unsteadiness of a separation bubble via time-resolved and scanning PIV measurements. *Exp Fluids* 45:675–691
- Burgmann S, Dannemann J, Schröder W (2007) Time-resolved and volumetric PIV measurements of a transitional separation bubble on an SD7003 airfoil. *Exp Fluids* 44:609–622
- Galbraith MC, Visbal MR (2008) Implicit large eddy simulation of low reynolds number flow past the SD7003 airfoil. In 46th AIAA Aerospace sciences meeting and exhibit, Reno, Nevada, 7–10 January, No. AIAA-2008-225
- Galbraith MC, Visbal MR (2010) Implicit large eddy simulation of low-reynolds-number transitional flow past the SD7003 airfoil. In 40th fluid dynamics conference and exhibit, Chicago, Illinois, 28 June–1 July, No. AIAA-2010-4737
- Gendrich CP, Koochesfahani MM (1996) A spatial correlation technique for estimating velocity fields using molecular tagging velocimetry (MTV). *Exp Fluids* 22:67–77
- Gendrich CP, Koochesfahani MM, Nocera DG (1997) Molecular tagging velocimetry and other novel applications of a new phosphorescent supramolecule. *Exp Fluids* 23:675–691
- Hill RB, Klewicki JC (1996) Data reduction methods for flow tagging velocity measurements. *Exp Fluids* 20:142–152
- Katz A (2010) Molecular tagging velocimetry measurements of the low-reynolds-number flow past the SD7003 Airfoil, M.S. Thesis, Mechanical Engineering Dept. Michigan State University, East Lansing, MI
- Koochesfahani MM, Nocera DG (2007) Molecular tagging velocimetry, *Handbook of experimental fluid dynamics*, Chap 5.4 Springer Berlin
- Matsubara M, Alfredsson PH (2001) Disturbance growth in boundary layers subjected to free-stream turbulence. *J Fluid Mech* 430:149–168
- Ol MV, McAuliffe BR, Hanff ES, Scholz U, Kähler C (2005) Comparison of laminar separation bubble measurements on a low reynolds number airfoil in three facilities. In 35th AIAA fluid dynamics conference and exhibit, Toronto, Ontario Canada, 6–9 June, No AIAA 2005-5149
- Olson D (2011) Facility and flow dependence issues influencing the experimental characterization of a laminar separation bubble at low reynolds number. M.S. thesis, Mechanical Engineering Dept. Michigan State University, East Lansing, MI
- Radespiel R, Windte J, Scholz U (2006) Numerical and experimental flow analysis of moving airfoils with laminar separation bubbles. In 44th AIAA Aerospace sciences meeting and exhibit, Reno, Nevada, 9-12 January, No. AIAA 501
- Visbal MR, Gaitonde DV (1999) High-order-accurate methods for complex unsteady subsonic flows. *AIAA J* 37(10):1231–1239
- Visbal MR, Gaitonde DV (2002) On the use of high-order finite-difference schemes on curvilinear and deforming meshes. *J Comput Phy* 181:155–185
- Visbal MR, Rizzetta DP (2002) Large-eddy simulation on curvilinear grids using compact differencing and filtering schemes. *J Fluids Eng* 124:836–847
- Visbal MR, Morgan PE, Rizzetta DP (2003) An implicit les approach based on high-order compact differencing and filtering schemes, AIAA Paper 4098